SPECTRAL UNMIXING APPLIED TO VEGETATED ENVIRONMENTS IN THE CANADIAN ARCTIC FOR MINERAL MAPPING

K. Staenz, C. Nadeau, J. Secker, and P. Budkewitsch

Canada Centre for Remote Sensing
588 Booth Street, Ottawa, Ontario, Canada K1A 0Y7
Phone: (613) 947-1250, Fax: (613) 947-1383, E-mail: karl.staenz@ccrs.nrcan.gc.ca

Working Group VII/1

KEY WORDS: Hyperspectral VNIR/SWIR Data, Vicarious Calibration, Atmospheric Correction, Automatic Endmember Selection, Spectral Unmixing, Lichen, Mineral Mapping, Canadian Arctic.

ABSTRACT

This paper shows preliminary results of mineral mapping under moderate tundra vegetation cover in an arctic environment. The data analysis including recalibration, atmospheric correction, automatic endmember extraction, and constrained linear spectral unmixing was applied to two hyperspectral image cubes acquired with the Probe-1 sensor over a test site in the Povungnituk Range in Northern Quebec, Canada. The mapping results indicate that different rock units (gabbro, basalt) could be identified successfully. However, the analysis also shows that the following factors impede the extraction of rock units: Lichen cover masks the reflectance of rock units, and sensor viewing angle and terrain influence the spectral signature (bidirectional reflectance). Ground reference information such as reference spectra of different target types, acquired during the data collection, were used to validate the unmixing results.

1 INTRODUCTION

Over the last 15 years, spectral unmixing techniques have been developed together with endmember selection procedures to successfully map minerals under sparse vegetation cover such as in arid and semi-arid regions of interest using hyperspectral data (Mustard and Pieters, 1986; Gillespie *et al*., 1990; Boardman and Huntington, 1996; Neville *et al*., 1998; Staenz *et al*., 1999). A particular challenge for mineral mapping is the application of these techniques to areas with increased vegetation condition. Accordingly, the objective of this study is to validate the use of spectral unmixing techniques for creating mineral abundance maps for geological mapping in an Arctic environment, located above the tree-line, but where other forms of vegetation are present. The study site is located in the Ungava Peninsula in northern Quebec, Canada (latitude 61-62 degrees). Bedrock exposure is fairly extensive in this region, but the immediate surface is heavily colonised by many species of crustose lichens and, to a lesser degree, by mosses and other vegetation. Therefore, unlike sparsely vegetated deserts in lower latitudes, the surface vegetation covers a larger proportion of the rock surfaces, which complicates the extraction of spectra related to the underlying rock required for the production of mineral maps.

Probe-1 data (Secker *et al.*, 2000) with a spatial resolution of 5 m and 128 bands between 440 nm and 2500 nm were acquired over the study site on July 28, 1998. The data are extensively pre-processed including calculation of new calibration coefficients using ground-based reflectance spectra and removal of atmospheric effects. Subsequently, an automatic endmember selection procedure is applied to the full band set in combination with a constrained linear spectral unmixing technique to map the minerals. These processing steps are being carried out using the Imaging Spectrometer Data Analysis System (ISDAS) developed at the Canada Centre for Remote Sensing (CCRS) (Staenz *et al*., 1998). This paper presents the first results of a study that is currently undertaken jointly by CCRS and several mining exploration companies.

2 SITE DESCRIPTION

The Povungnituk Range of the Ungava Peninsula lies within the Low Arctic ecozone, and is underlain by continuous permafrost. Landforms in relief are largely controlled by bedrock resistance to glaciation, which ended about 7500 years ago (Lauriol and Gray, 1987). Glacial deposits up to several meters thick in low lying areas locally developed a thin soil horizon. In these areas, a flora of small shrubs, rarely taller than 0.5 m, and over 160 taxa of smaller vascular plants are found (Dion *et al*., 1999). An equally great diversity of lichens are

found dwelling on both soil and rock surfaces. Geologically, the area lies within the Cape Smith Belt, a deformed Proterozoic greenstone belt that consists mainly of a thick sequence of basalts, intruded by mafic to ultramafic bodies (St-Onge and Lucas, 1993). Of interest to mineral exploration, the Belt hosts several occurrences of metallic sulfides, some of which contain economic quantities of Nickel, Copper and Platinum group elements being mined today.

3 DATA ACQUISITION AND PRE-PROCESSING

3.1 Ground-based reflectance spectra

Field measurements done during the same week as the airborne overflight included the acquisition of ground-based reflectance spectra using the GER3700™ portable field spectrometer. This instrument was configured with a 10-degree field-of-view (FOV) lens, giving a 0.26-m diameter ground FOV from a height of 1.5 m. Reference scans of a Spectralon™ panel were made to determine irradiance conditions, and these were used to convert target measurements to reflectance. All measurements were made while the sky was free of all clouds in the vicinity of the sun. The resulting reflectance spectra were corrected for the wavelength and angular dependency of the reference panel's reflectance (Secker *et al*., 2000). Finally, multiple measurements of a given sample were averaged to yield a mean spectrum for that sample.

3.2 Airborne hyperspectral Probe-1 data

The hyperspectral data for this study was obtained with the Probe-1 sensor on 28 July 1998. The mission parameters are summarized in Table 1. The Probe-1 sensor has 128 spectral bands spanning the wavelength range from 440 nm to 2500 nm, with bandwidths between 11 nm and 22 nm (Secker *et al*., 2000). It has a 60-degree FOV, which for the altitude of this mission corresponds to a swath width of about 3.0 km and 5-m pixels (Table 1). This sensor is mounted on a three-axis gyro-stabilized platform that compensates for the effects of the aircraft motion for up to 5 degrees for each axis.

The Probe-1 raw data was dark subtracted and trimmed to a width of 512 pixels (across track) to remove the dark current and calibration lamp pixels. Laboratory radiometric and spectroscopic coefficients were used to convert the raw data from digital numbers (DN) to radiance, with units of $\mu W\ cm^{-2}\ nm^{-1}\ sr^{-1}$. Then from the full flight line, two 512-by-512 pixel scenes were extracted for further analysis.

The raw at-sensor radiance spectra were converted to surface reflectance via an atmospheric correction using the MODTRAN3 radiative-transfer code (Berk *et al*., 1989; Anderson *et al*., 1995) implemented using a LUT approach in ISDAS (Staenz and Williams, 1997). Inputs to MODTRAN3 include mission-specific and sensor-specific parameters, and model-specific choices for atmospheric properties. These are summarized in Table 1. Using MODTRAN3, the atmospheric transmission was calculated over the full spectral range of the sensor, and resampled to match the characteristics of the Probe-1 sensor.

Date	1998-07-28
GMT	17:19:00
Aircraft heading	201°
Sensor tilt angle	0°
Sensor altitude (above sea level)	2.650 km
Pixel size	5 m
Atmospheric model	Subarctic summer
Aerosol model	Continental (rural)
Solar zenith angle	42.88°
Solar azimuth angle	185.48°
Terrain elevation (above sea level)	0.470 km
Water vapour	1.15 g/cm^2
Ozone column	0.346 cm-atm
CO_2 mixing ratio	357.5 ppm
Visibility	50 km

Table 1. Mission and MODTRAN3 model parameters for the atmospheric correction of the Probe-1 data.

Note that the default quantity of atmospheric water vapour for the Subarctic summer model was replaced by a value estimated from the data themselves, using a method which models the combined strength of the 940 nm and 1130 nm water vapour absorption lines in the spectra (Gao and Goetz, 1990; Green *et al*., 1991; Staenz and Williams, 1997). Inspection of pixels scattered throughout the image cubes showed that the variation in atmospheric water vapour was small (0.05 g/cm^2), and an average value of 1.15 g/cm^2 was used for both image cubes.

3.3 Correcting the laboratory calibration

Small errors in the spectral registration of the hyperspectral sensor were detected by analyzing the behaviour of the corrected surface reflectance spectra in the vicinity of strong atmospheric absorption features. The results of a spectral misregistration are then visible in the reflectance spectrum as a characteristic over and under correction of atmospheric absorption features. Then, the wavelength shifts were calculated which best corrected the reflectance to obtain a smooth spectrum in the vicinity of these absorption features. This process was applied separately for each of the four spectrometers in the Probe-1 sensor, resulting in shifts between -2.5 nm and -1 nm for the visible and near-infrared (VNIR) spectrometers.

To check the laboratory radiometric calibration for the Probe-1 sensor, reflectance spectra extracted from a Probe-1 scene for the Kattiniq-Donaldson airstrip were compared with field reflectance spectra of the airstrip, acquired using the GER3700^{TM} simultaneously with the overflight. This airstrip is surfaced with glacial drift (composed of clay, sand and gravel packed together), and it appeared to be a homogeneous mixture of the constituent materials on a scale of a few meters. Comparison of these spectra revealed that the laboratory radiometric coefficients were significantly in error throughout the full spectral range of the sensor. Therefore, a reflectance-based vicarious calibration (RBVC) method was used to adjust the Probe-1 radiometric calibration coefficients (Secker *et al*., 2000). This is an iterative numerical technique that adjusts the radiometric coefficients to reduce the absolute difference between the ground-based (calibrating) reflectance spectrum and the reflectance spectrum extracted from the hyperspectral data to within a specified tolerance (0.02 percent absolute in this case). The RBVC method yields a corrected set of radiometric coefficients that convert the hyperspectral data from DN to radiances. These corrected coefficients, along with the corrections to the spectral registration, were applied to the Probe-1 raw data to yield radiance. These new radiance cubes were atmospherically corrected (as described in Section 3.2) prior to the analysis presented in Sections 4 and 5.

4 ENDMEMBER SELECTION AND SPECTRAL UNMIXING

To map proportions of rock types and vegetation, a constrained linear spectral unmixing technique is used (Adams *et al*., 1986; Shimabukuru and Smith, 1991; Boardman, 1995). Spectral unmixing uses a linear combination of a set of spectra, called endmembers, to unmix the composite spectrum into endmember fractions (between 0 and 1) for each pixel of the image cube. Endmembers needed for the unmixing can be selected in different ways. Library spectra can be used to unmix a scene or endmembers can be selected directly from the image cube. Using the extremities of the n-dimensional data cloud (where n is the number of spectral bands) formed by a principal component transform of the reflectance cube, a set of endmembers can be extracted (Boardman, 1995). This manual method can be time consuming and finding significant extremities of the data cloud can be a difficult task. A new method has been developed at the CCRS to automatically extract endmembers directly from the imagery, without having to previously transform the data in any way. This method is called Iterative Error Analysis (IEA) and is described in detail by Szeredi *et al*. (1999). To start, the average spectrum of the scene is used to unmix the dataset. When a dataset is unmixed, a residual error image is produced. These errors are calculated using a least-square estimate between the average spectrum and the spectrum of each pixel. These errors are also a measure of the distance between the average spectrum and all the spectra of the dataset. The next step is to find the pixel or pixels that encompass the largest errors, i.e., that are furthest away from the average spectrum. The user provides the number of pixels forming these endmembers. This new endmember is then used to unmix the image cube, and the average spectrum is discarded. The errors will again be used to find the furthest pixels from the first endmember and will create the second endmember. This process is repeated until the number of endmembers predetermined by the user is reached.

For the two image cubes used for this paper, 20 endmembers were extracted and each of these was composed of a maximum of 25 pixels. The full spectral range of the Probe-1 sensor was utilised for the endmember selection and spectral unmixing. Once all the endmembers were found, the image cubes were unmixed using the endmembers and a fraction image is produced for each endmember. Examples of these fraction images are shown in Figures 1 and 2.

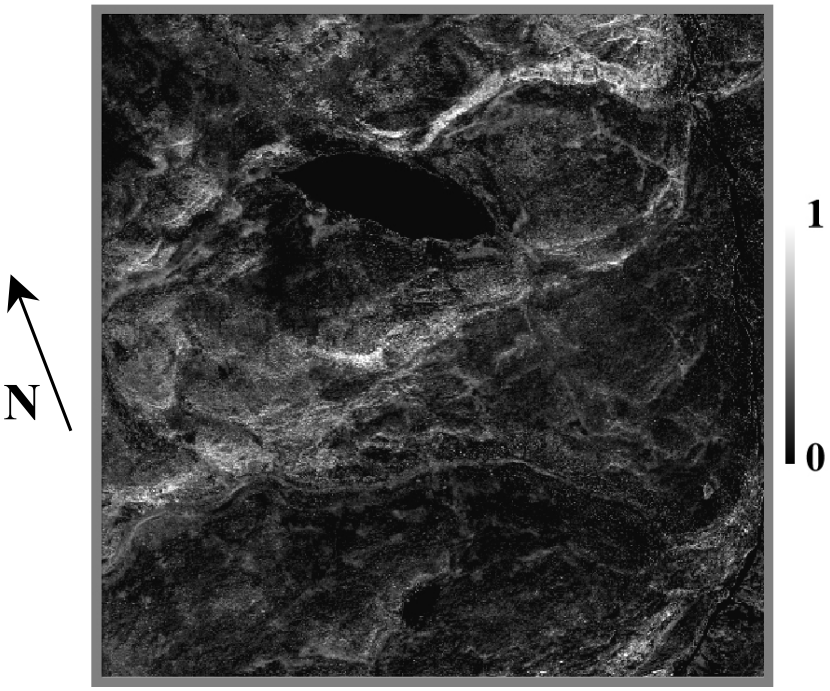

Figure 1. Summed fraction image of endmembers 9, 10 and 15 (gabbro-pyroxenite sill) for the first image cube.

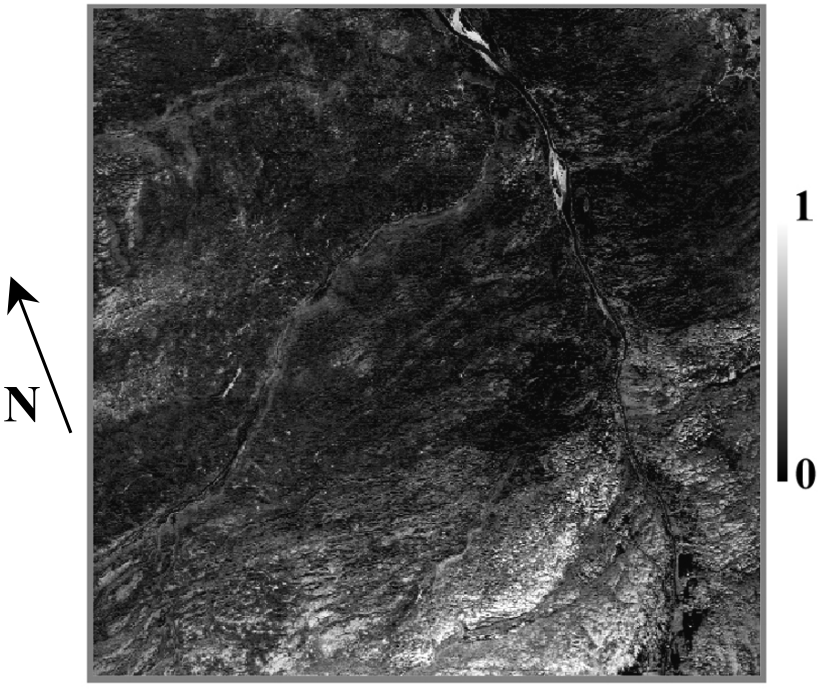

Figure 2. Summed fraction image of endmembers 8 and 10 (metamorphosed basalt with lichen cover) for the second image cube.

5 RESULTS AND DISCUSSION

For this study, two image cubes were processed and the results are presented in Figures 1-6. Of the 20 endmembers extracted using the IEA method from each of these cubes, only a few are of geological interest. Those are metamorphosed basalt and gabbro-pyroxenite (first image cube) as well as metamorphosed basalt and high grade of metamorphic rocks (second image cube). Other endmembers are common tundra vegetation types, water, snow and shadow. Because of bidirectional effects caused by local variations in the topography, the IEA procedure extracted spectrally similar endmembers that were only differentiated by their amplitudes. At this time, a digital elevation model was not used to help correct for these effects. Accordingly, these spectrally similar endmembers were averaged and the corresponding fraction images were added. Examples of Probe-1 rock and vegetation endmembers that match well with the corresponding ground-based reflectance spectra are illustrated in Figures 3-6. Our study, however, focuses on the geological significance of the endmember extraction and analysis of fraction images produced by spectral unmixing.

To yield the map of the first image cube presented in Figure 1, three fraction images were summed An average spectrum of these three endmembers is presented in Figure 3 with a GER3700^{TM} measurement of pyroxenite. Ground-based reflectance spectra indicate that the automatic IEA endmember extraction procedure is not able to find the spectral signature of a pure rock pixel. This might be caused by the ubiquitous lichen cover that can be seen in an absorption feature near 2100 nm in the dashed curves shown in Figure 3. As well, the spatial resolution of these image cubes (5-m pixels) might not be sufficiently small to generate pure pixels. In spite of this limitation, general characteristics on two rock endmembers identified can be described. Several minerals present in the rock, such as chlorite, amphibole, pyroxene, serpentine and talc, and combinations thereof, can explain the relatively narrow absorption doublets at about 2310 nm and 2380 nm observed in one of the extracted endmembers (Figure 5), likely a gabbro-pyroxenite sill. A relatively lichen-free pyroxenite rock surface measured on the ground exhibits similar characteristics to the endmember identified as corresponding to gabbro-pyroxenite sills. Two sills are known to cross (diagonally) the area shown and are broadly identified in the fraction image (Figure 1). The highest fractions appear along south (sun-facing) edges of small topographic ridges. The streaking toward the upper left in the fraction image is oriented to the NW direction, resulting from glacier movement in this area.

The fraction image from the second image cube as shown in Figure 2 corresponds extremely well to the mapped distribution of a metamorphosed basalt, confined to the lower right side. To produce this map, two fraction images were summed. The two endmembers used to produce this fraction image are averaged to yield the spectrum in Figure 6 together with GER3700^{TM} spectra of basalt and black lichen (genus *Sporastatia*). This average endmember spectrum exhibits absorption features of lichen and basalt, notably around 2100 nm and 2380 nm, which again demonstrates that no pure basalt pixels were available in the dataset to be extracted by the IEA method. The rock unit identified in the summed fraction image is chiefly composed of chlorite and plagioclase, typically 60 to 90 percent coated by various crustose and foliose lichens. A single broad absorption feature centred near 2340 nm may well correspond to the combined absorption features in lichens and chlorite, as well as other minerals. It is interesting to note the gravel bars located along the north flowing river, dissecting the area (Figure 2). On these gravel bars, there is a high proportion of basalt, identified by high fractions, that appear to have been carried down stream from their source area.

6 CONCLUSIONS AND RECOMMENDATIONS

A preliminary investigation indicates that endmember analysis of hyperspectral data can be successful at identifying different rock units in tundra environments of the Arctic. However, from our analysis of these hyperspectral datasets, it was found that three important factors impede the automatic endmember extraction procedure and subsequent spectral unmixing of hyperspectral data. These are:

1- Dense saxicolous lichen cover effectively masks the spectral reflectance characteristics of underlying bedrock in the 400-2500 nm wavelength range, at the 5-m pixel scale of the hyperspectral data. However, it is possible that some rock types can be distinguished based on the spectral characteristics of the rock combined with those of the lichen cover. As well, some rock types are prone to lichen cover, whereas others are more barren.

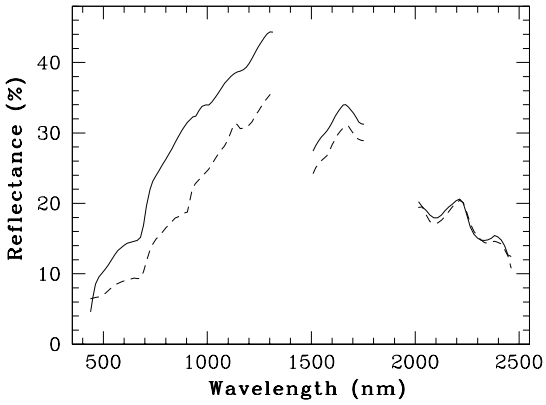

Figure 3: Spectrum of Probe-1 endmember 11 (dashed line) and a GER3700^{TM} spectrum of lichen (solid line).

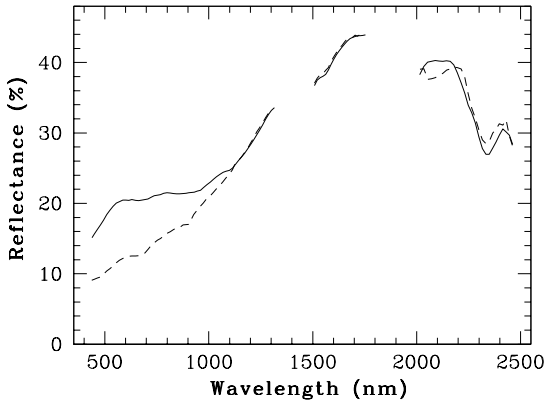

Figure 4: Spectrum of Probe-1 endmember 2 (dashed line) and a GER3700^{TM} spectrum of metamorphosed basalt (solid line).

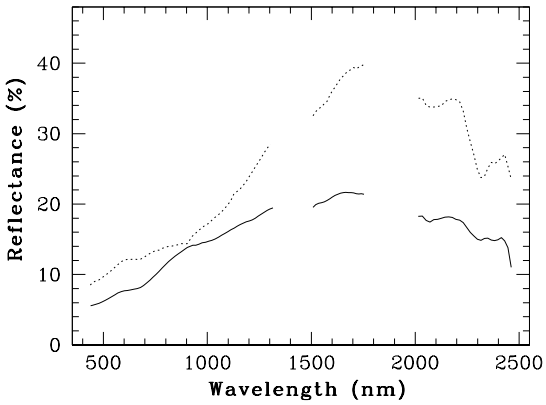

Figure 5: Average spectrum of Probe-1 endmembers 9, 10 and 15 (dotted line) and a GER3700^{TM} pyroxenite spectrum (solid line).

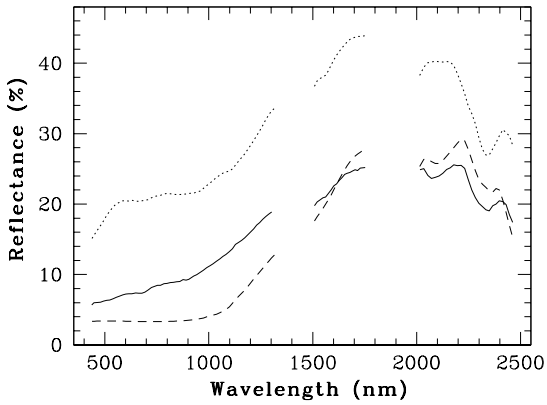

Figure 6: Average spectrum of Probe-1 endmembers 8 and 10 (solid line) and GER3700^{TM} spectra of black lichen (dashed line) and basalt (dotted line).

2- Bidirectional reflectance has a profound effect on the types of endmember spectral signatures extracted from the data. This is due to the low solar elevation angles (<45°) in the arctic combined with variable slope and aspect of the terrain and finally the 60° FOV of the Probe-1 sensor.
3- Glaciation has dispersed blocks of bedrock from their original source area, causing a natural mixing of endmember material on the ground, which further complicates the understanding of the unmixing results.

ACKNOWLEDGEMENTS

The authors wish to thank J. Gingerich (Noranda Mining and Exploration Inc.) and R. Moore (Falconbridge Limited) for making the Probe-1 data over the Kattiniq-Donaldson airstrip available to CCRS. Thanks to M. Peshko (Noranda Mining and Exploration Inc.), L. McBean and J. Wong (Falconbridge Limited) for their technical support. The authors acknowledge the financial support of Barrick Gold Corp., Cameco, Cominco Ltd., De Beers Consolidated Mines Ltd., Falconbridge Limited, Noranda Mining and Exploration Inc., and Placer Dome Exploration Inc. Thanks to R. Neville (CCRS) for providing a careful review of the manuscript.

REFERENCES

Adams, J.B., Smith, M.O., and Johnson, P.E., 1986. Spectral Mixture Modelling: A New Analysis of Rock and Soil Types at the Viking Lander 1 Site. Journal of Geophysical Research, 91, pp. 8098-8112.

Anderson, G.P., Wong, J., and Chetwynd, J.H., 1995. MODTRAN3: An Update on Recent Validations Against Airborne High Resolution Interferometer Measurement. Summaries of the Fifth Annual JPL Airborne Earth Science Workshop, Jet Propulsion Laboratory, JPL Publication 95-1, Vol. I, pp. 5-8.

Berk, A., Bernstein, L.S., and Robertson, D.C., 1989. MODTRAN: A Moderate Resolution Model for LOWTRAN7. Final Report, GL-TR-0122, AFGL, Hanscom AFB, Maryland, USA, 37 pages.

Boardman, J.W., 1995. Analysis, Understanding and Visualization of Hyperspectral Data as Convex Sets in n-Space. Proceedings of the International SPIE Symposium on Imaging Spectrometry, SPIE Vol. 2480, Orlando, Florida, U.S.A., pp. 23-36.

Boardman, J.W., and Huntington, J.F., 1996. Mineral Mapping with 1995 AVIRIS Data. Summaries of the Sixth Annual JPL Airborne Earth Science Workshop, Pasadena, California, U.S.A., JPL Publication 96-4, Vol. 1, pp. 9-11.

Dion, L., Cayouette, J., and Deshaye, J., 1999. La flore vasculaire de la region des Monts D'Youville et de Puvirnituk, Nunavik, Quebec nordique. Provancheria, 27, Universite Laval, Quebec, 67 pages.

Gao, B.-C., and Goetz, A.F.H., 1990. Column Atmospheric Water Vapour and Vegetation Liquid Water Retrievals from Airborne Imaging Spectrometer Data. Journal of Geophysical Research, 95(D4), pp. 3549-3564.

Gillespie, A.R., Smith, M.O., Adams, J.B., Willies, S.C., Fischer, A.F., and Sabol, D.E., 1990. Interpretation of Residual Images: Spectral Mixture Analysis of AVIRIS Images, Owens Valley, California. Proceedings of the Second Airborne Visible/Infrared Imaging Spectrometer (AVIRIS) Workshop, Pasadena, California, JPL Publication 90-54, pp. 243-270.

Green, R.O., Conel, J.E., Margolis, J.S., Brugge, C.J., and Hoover, G.L., 1991. An Inversion Algorithm for Retrieval of Atmospheric and Leaf Water Absorption from AVIRIS Radiance with Compensation for Atmospheric Scattering. Proceedings of the Third Annual JPL Airborne Earth Science Workshop, Pasadena, California, JPL Publication 91-28, Vol. I, pp. 51-61.

Lauriol, B., and Gray, J.T., 1987. The decay and disappearance of the Late Wisconsin ice sheet in the Ungava Peninsula, northern Quebec, Canada. Arctic and Alpine Research, 19, pp. 109-126.

Mustard, J.F., and Pieters, C.M., 1986. Abundance and Distribution on Mineral Components Associated with Moses Rock (Kimberlite) Diatreme. Proceedings of the Second Airborne Imaging Spectrometer Data Analysis Workshop, Pasadena, California, JPL Publication 86-35, pp. 81-85.

Neville, R.A., Nadeau., C., Levesque, J., Szeredi, T., Staenz, K., Hauff, P., and Borstad, G.A., 1998. Hyperspectral Imagery for Mineral Exploration: Comparison of Data from Two Airborne Sensors. Proceedings of the International SPIE Symposium on Imaging Spectrometry, San Diego, California, SPIE Vol. 3438, pp. 74-82.

Secker, J., Staenz, K., Gauthier, R.P., and Budkewitsch, P., 2000. Vicarious Calibration of Hyperspectral Sensors in Operational Environments, Remote Sensing of Environment, submitted.

Shimabukuru, Y.E., and Smith, J.A., 1991. The Least Squares Mixing Models to Generate Fraction Images Derived From Remote Sensing on Multispectral Data. IEEE Transactions on Geoscience and Remote Sensing, 29, pp. 16-20.

St-Onge, M.R., and Lucas, S.B., 1993. Geology of the eastern Cape Smith Belt: Parts of the Kangiqsujuaq, cratere du Nouveau-Quebec, and lacs Nuvilik map areas, Quebec. Geological Survey of Canada, Memoir 438, 110 pages.

Staenz, K., and Williams, D.J., 1997. Retrieval of Surface Reflectance from Hyperspectral Data Using a Look-Up Table Approach. Canadian Journal of Remote Sensing, 23(4), pp. 354-368.

Staenz, K., Szeredi, T., and Schwarz, J., 1998. ISDAS - A System for Processing/Analyzing Hyperspectral Data. Canadian Journal of Remote Sensing, 24(2), pp. 99-113.

Staenz, K., Neville, R.A., Levesque, J., Szeredi, T., Singhroy, V., Borstad, G.A., and Hauff, P., 1999. Evaluation of *casi* and SFSI Hyperspectral Data for Environmental and Geological Applications – Two Case Studies. Canadian Journal of Remote Sensing, 25(3), pp. 311-322.

Szeredi, T., Staenz, K., and Neville, R.A., 1999. Automatic Endmember Selection : Part I Theory. Remote Sensing of Environment, submitted.